Three-Dimensional Particle Simulations of Ion Optics Plasma Flow

J. Wang, J. Anderson, and J. Polk

Jet Propulsion Laboratory

California Institute of Technology, Pasadena

1. Introduction

More than 30 years after its inception, ion propulsion is finally being considered for practical applications. Under NASA's NSTAR (NASA Solar electric propulsion Technology Application Readiness) program, xenon ion propulsion technology is being validated for use on planetary and commercial spacecraft. The New Millennium Deep Space One (DS1) spacecraft, scheduled for launch in October 1998, will be the first ever interplanetary spacecraft using an ion thruster (developed under the NSTAR program) as its primary propulsion system.

A key part of the NSTAR activity is to validate the service life capability of the NSTAR ion engine. This is being accomplished by a combination of endurance tests and by developing a probabilistic analysis methodology to determine the ion engine failure risk as a function of engine run time. As part of the service life capability assessment of the NSTAR ion engine, a model which predicts the characteristics of the plasma flow in ion optics is needed. This paper discusses our ongoing work of developing a fully 3-dimensional ion optics plasma flow model and applying this code in the analysis of the results from the 8000 hour NSTAR ion thruster endurance test.

Ion optics plasma flow has been a subject of numerous studies. The nature of this problem has rendered computer particle simulation, which solves plasma particle trajectory, space charge, and the Poisson's equation self-consistently, as the preferred modeling method. Some recent ion optics simulation studies can be found in Arakawa and Nakano[1996], Hayakawa[1992], Peng et al.[1991,1992,1994], Bond and Latham[1995], Shiraishi et al.[1995], etc and references therein. For instance, Bond and Latham[1995] and Shiraishi et al.[1995] developed 2-dimensional (2-D) axisymmetric particle-in-cell with Monte Carlo collision (PIC-MCC) codes which uses a cylindrical grid and a finite-difference method to solve the Poisson's equation. The axisymmetric formulation is not able to take into account of the hexagonal layout of the aperture array. Arkawa and Nakano[1996], Hayakawa[1992], and Peng et al.[1994] developed 3-dimensional (3-D) PIC-MCC codes which use a triangular mesh to handle the optics aperture geometry. and a finite-element method to solve the Poisson's equation. Most 3-D simulation models are designed for a single grid aperture by considering the six-fold hexagonal symmetry of the aperture array. Due to computational constraints, 3-D simulations of a single aperture are typically performed for a cross section of one twelfth of a single aperture (30 degree by 60 degree right-triangle cross section).

In this current study, we attempt to develop a more generalized, fully 3-D PIC-MCC code. The code is designed in such a way that not only single aperture but also multiple apertures can be included explicitly in the simulation domain. The option to explicitly include multiple apertures is important because our eventual goal is to peform global simulations of ion thruster aperture arrays. Complex geometries such as that associated with the ion optics are best handled by tetrahedral cells or unstructured grids and finite-element based formulations. However, a tetrahedral cell based or unstructured grid based PIC code can be significantly computationally more expansive than a standard orthogonal grid PIC code. In a standard orthogonal grid PIC code, the location of memory of quantities defined in neighboring cells can be found trivially via indexing. This is in contrast to an unstructed grid where the neighbors of a given cell must be found by lookups in a table or other methods requiring additional memory references. More over, for either tetrahedral cells or unstructured grids, a fairly complex scheme is typically needed to determine a particle's new cell [Westermann, 1992]. These added complexities can make large-scale 3-D ion optics simulations prohibitively expansive be-

cause a PIC code typically spends most of its computing time pushing particles and performing particle-grid interpolations. Out of considerations for computational efficiency for large-scale simulations, the current code is build upon the standard orthogonal grids and a finite-difference based formulation[Wang,1998]. To accommodate the complex geometry associated with the optics apertures, a method of sub-gridscale placement of boundaries [Grote,1994] is used. This method explicitly includes the location of the optics wall in relation to the grid in the finite-difference form of Poisson's equation. We find that such an approach is sufficient for this particular problem and allows us to retain the computational efficiency associated with an orthogonal grid PIC code.

This code, while not completely finished yet, is currently being applied to help the analysis of the results from the 8000 hour test of the NSTAR ion thruster. In this paper, we will also discuss an ongoing application study of the onset of electron backstreaming, which is a potential failure mode for the NSTAR ion engine.

NSTAR ion thrusters operate by accelerating propellant ions through a molybdenum, two-grid ion optics system. The discharge chamber anode is biased to a specified voltage to give the desired specific impulse. The screen grid, located at the upstream end of the discharge chamber, is biased at discharge chamber cathode potential and is designed to focus ions through the accelerator grid apertures. The accelerator grid, located downstream of the screen grid, is biased negative to extract discharge chamber ions. In addition to providing the ion-accelerating electric field, the accelerator grid must provide a potential barrier to keep beam neutralizing electrons, injected downstream of the optics system, from traveling upstream (backstreaming) into the discharge chamber. It has been observed that the magnitude of the voltage required to prevent electron backstreaming will increase during the life of the thruster. This occurs because the accelerator grid apertures enlarge as a result of sputter erosion caused by direct impingement of a small fraction of the beamlet ions which are not properly focused through the ion optics and by charge-exchange ions produced downstream of the screen grid [Rawlin, 1993]. Electron backstreaming is undesirable because it reduces the thruster efficiency; each electron which backstreams into the discharge chamber consumes as much power as a singly-ionize propellant ion but does not produce thrust. The electron energy is deposited as thermal energy in the discharge chamber. If the backstreaming current is large enough, the discharge chamber can overheat and degrade the permanent magnets required for efficient discharge chamber operation. While most previous studies of ion optics plasma flow have concentrated on the grid erosion problem, simulation studies of electron backstreaming have not been previously reported.

Section 2 discusses the simulation mode and presents results from an example simulation. Section 3 discusses an analysis of electron backstreaming. Section 4 contains a summary and conclusions.

2. Simulation Model

The main part of the simulation model is a particle-ion Boltzmann-electron PIC-MCC code for simulations on ion time scale, which has a formulation similar to other ion optics codes. In this code, the ions are represented by individual test particles and the electrons are assumed to have a fluid response in which the density is approximated by the barometric law. The electric field, space charge, and ion trajectories are solved self-consistently from the Poisson's equation

$$\nabla^2\Phi = -4\pi(n_i - n_e) \tag{1}$$

and the Newtown's second law

$$\frac{dm\vec{V}}{dt} = \vec{F} = q\vec{E}, \quad \frac{d\vec{x}}{dt} = \vec{V} \tag{2}$$

A typical simulation setup is shown in Fig.1. The simulation domain can be setup to include single as well as multiple apertures. Since we have only implemented symmetric boundary condition, currently the simulation boundaries can be taken on any of the "symmetric" surfaces. The "minimum" simulation cross section will be a cross section including two quarter-size holes. Note that this minimum cross section fully accounts for the geometric effects from a hexagon layout of the aperture arrays.

Along the acceleration direction (z direction), the upstream boundary represents the discharge chamber plasma, which has a plasma potential Φ_0, density n_0, and and electron temperature T_{e0}. We make no assumptions about the upstream screen grid plasma sheath. The extracted ion current is determined self-consistently from the acceleration voltage and the upstream plasma boundary condition.

The downstream boundary represents the neutralized propellant plasma, which has a plasma potential Φ_∞, density n_∞, and electron temperature $T_{e\infty}$. We define a quasi-neutral zone near the downstream boundary within which we assume that the propellant ions are neutralized. Currently we only include the propellant plasma in our downstream condition. Hence, the

downstream density n_∞ is determined by the propellant ions. We take the downstream plasma density to be the average beam ion density within the quasi-neutral zone. Hence, unlike other boundary parameters, the downstream density n_∞ is updated at every time step.

A Boltzmann relationship between the electron density and local electrostatic potential is assumed for both the regions upstream of the screen grid and downstream of the acceleration grid. Specifically, the electron density in the region upstream of the screen grid is given by

$$n_e = n_0 \exp(\frac{\Phi - \Phi_0}{T_{e0}}), \quad \Phi < \Phi_1 \tag{3}$$

$$n_e = n_0(1 + \frac{\Phi - \Phi_0}{T_{e0}}), \quad \Phi > \Phi_1 \tag{4}$$

and the electron density in the region downstream of the acceleration grid is given by

$$n_e = n_\infty \exp(\frac{\Phi - \Phi_\infty}{T_{e\infty}}), \quad \Phi < \Phi_\infty \tag{5}$$

$$n_e = n_\infty(1 + \frac{\Phi - \Phi_\infty}{T_{e\infty}}), \quad \Phi > \Phi_\infty \tag{6}$$

At each time step, the propellant ions are injected into the simulation domain from the upstream boundary. The upstream density and injection velocity are the input variables to control the extracted ion current. In order to have a stable sheath solution, the ions are injected into the domain with the Bohm velocity. Each ion particles moves according to eq(2) until a charge-exchange collision has occurred. The probability that a charged particle suffers a collision within time t is given by

$$P(t) = 1 - \exp(-\int_0^t \nu(t)dt) \tag{7}$$

where $\nu = n_n(\vec{x})v\sigma(v)$ is the collision frequency. For charge exchange collisions, the empirical relationship[Rapp,1962; Bond and Latham,1995]

$$\sigma = (a - b\ln(v))^2 \tag{8}$$

is used. Since the neutral density, which is defined on grid points, is nonuniform, the collision frequency for each particle is obtained by interpolating the neutral density $n_n(x, y, z)$ to the particle position, similar as the field interpolation in a PIC code. At each time step, for each particle, the accumulated collision probability in the time step is calculated, and a random number P_{ran} evenly distributed between 0 and 1 is then chosen to determine whether a collision has occurred.

The neutral density is calculated by a neutral particle code, which is similar to that by Bond and Latham[1995] and Peng et al.[1994]. In the code, the neutrals are assumed to undergo a free molecular flow. When the neutral particles hit the optics walls, they undergo a diffuse reflection.

As stated in the introduction, we have decided to build our simulation code on orthogonal grids rather than more sophisticated grids, such as unstructured grids or tetherdral cells, out of computational efficiency considerations. To match the optics wall boundary, we adopt a method of sub-gridscale placement of boundaries, as shown in Fig.2. This method explicitly includes the location of the optics wall in relation to the grid in the finite-difference form of Poisson's equation. This method, which is first described in [Grote,1994], can be easily illustrated with the finite-difference form of 1-D Poisson's equation:

$$\frac{\Phi_{i+1} - 2\Phi_i + \Phi_{i-1}}{h^2} = -\rho_i \tag{9}$$

Let's consider that the edge of a conductor surface is between grid points i and $i+1$, where grid point i is outside the conductor and grid point $i+1$ is inside the conductor. The distance between the conductor surface and grid point i is δ. We assume that the potential at the edge would be interpolated linearly

$$\Phi_{edge} = (1 - \delta)\Phi_i + \delta\Phi_{i+1} \tag{10}$$

Note that Φ_{edge} is the known surface potential of the conductor and Φ_{i+1} is a free parameter since it is inside the conductor. By substituting Φ_{i+1} in eq(9) with the above interpolation relation: $\Phi_{i+1} = (\Phi_{edge} - (1 - \delta)\Phi_i)/\delta$, we obtain the finite difference equation at conductor surface

$$\frac{-(2 + (1 - \delta)/\delta)\Phi_i + \Phi_{i-1}}{h^2} = -\rho_i - \frac{\Phi_{edge}}{h^2} \tag{11}$$

Note that in the above equation, Φ_i approaches Φ_{edge} as $\delta \to 0$. This method extends easily to three dimensions. The linear interpolation is done independently in each direction for which there is a conductor.

The results from a typical run are shown in Figures 3 to 8. This run is performed for a domain which includes 2 quarter-size apertures. A cross section of the simulation domain at the accelerator grid is shown in Fig.3. For this test case runs, the number of cells used are $25 \times 25 \times 71$ and the average number of test particles used are about 0.3 million particles.

This simulation is performed for nominal geometric and operating conditions of the NSTAR ion engine,

screen hole diameter d_s	1.91 mm
screen grid thickness t_s	0.38 mm
accel hole diameter d_a	1.14 mm
accel grid thickness t_a	0.51 mm
screen to accel grid gap g	0.58 mm
center-to-center hole spacing l	2.21 mm
beamlet current	0.27 mA/hole
total accelerating voltage	1100 V
screen grid voltage	1070 V
accel grid voltage	-180 V

Table 1: Nominal geometric and operating parameters for the NSTAR ion engine

listed in Table 1. The upstream plasma boundary condition is taken to be $\Phi_0 = 1100$V and $T_{e0} = 5$eV, and the downstream plasma condition $\Phi_\infty = 0$V and $T_{e\infty} = 1.5$eV.

Fig.4 shows the potential contours on three cutting surfaces: a x-y cutting plane at a distance of about 0.045mm downstream of the accelerator grid, the z-x surface at $y = 0$, and the z-y surface at $x = 0$. Figures 5 and 6 are snapshots of those primary beam ions and charge-exchange ions within one grid cell of the z-x surface at $y = 0$. Figures 5a and 6a show the positions of primary beam ions and charge-exchange ions, respectively, and Figures 5b and 6b show their z vs. v_z phase space. Fig.6b shows that there are two distinct populations of charge exchange ions, one of the populations matches the one for the primary beam ions. This population of charge-exchange ions originate from charge-exchange collisions upstream of the accelerator grid, and are indistinguishable from the beam ions. The second population are generated downstream of the accelerator grid. These ions will back flow towards the accelerator grid, and are responsible for grid erosion. Fig.7 shows the ion current density vector and ion velocity vector on the z-x surface at $y = 0$.

3. Electron Backstreaming

The 3-D ion optics models described in the last section is currently being applied in the analysis of the results from NSTAR long endurance test. An ongoing study focuses on electron backstreaming.

During normal operations, the accelerator grid provides a potential barrier which keeps the neutralizing electrons from traveling upstream (backstreaming) into the discharge chamber. As will be discussed later, this potential barrier is determined by the potential at a "saddle" point near the center of the accelerator grid aperture rather than the accelerator potential. The saddle point potential, Φ_s, is at a higher value than the accelerator voltage. The potential barrier is influenced by at least 14 independent parameters. They include the six geometric parameters related to the ion optics (the screen and accelerator grid thicknesses, the diameter of the screen and accelerator grid holes, the hole-to-hole spacing for the grids and the spacing between the grids), the six plasma parameters related to the discharge chamber plasma and the charge exchange plasma produced downstream of the ion optics system (plasma density, electron temperature, and plasma potential), and the screen grid and accelerator grid voltage. In addition, other factors, such primary electrons in the discharge chamber plasma or the cusp shape resulting from the acid etching of the ion optics system holes, may also play a role. For a given thruster design, the accelerator grid voltage, the accelerator grid hole diameter, the spacing between the grids, the ion current per hole, and the electron temperature in the plasma downstream of the accelerator grid are expect to play a particularly important role. As noted previously, accelerator grid aperture will enlarge by ion sputtering. The gap between the grids will vary during ion thruster startup transient period as well as in flight when the thruster's thermal environment changes. Investigation of the quantitative effects of these five parameters is a first step in developing an electron backstreaming model for two-grid ion optics systems.

Although electron backstreaming occurs through the entire ion optics apertures, our initial effort is to investigate the effect of these parameters on electron backstreaming through a single accelerator grid aperture. To understand the onset of electron backstreaming, one first needs to examine in detail the structure of the electric field near the accelerator grid.

Several sets of parametric simulations are performed to cover a range of accelerator voltages, beamlet currents, accelerator hole diameters, and grid gaps. Potential contour maps from some of these parametric simulations are shown in figures 9 through 13. A common feature in these potential contour maps is the existence of a "saddle" point, which is the location on the aperture axis where a potential contour originated from upstream of accelerator grid intersects a potential contour of the same value originated from the downstream region It is obvious that the saddle potential potential Φ_s represents a potential barrier or a "gate" for the downstream

electrons: those electrons with an energy larger than Φ_s will be able to go through the saddle point and flow backwards through the accelerator system. Hence, we investigate the conditions under which the Φ_s becomes high enough to permit a sufficient number of electrons to backflow.

The result in Fig.9 is for the nominal geometric and operating parameters of the NSTAR engine listed in Table 1. In figures 10 and 11, we keep the same geometric parameters (accelerator hole diameter: $d_a = 1.14$mm; grid gap: $g = 0.58$mm) but vary the beamlet current and accelerator voltage. Fig.10 shows the results for different beamlet currents. In Fig.10a, there is no beamlet current and potential contours are from the solution of the Laplace equation. In Fig.10b, the beamlet current is taken to be 0.21 mA/hole. Fig.11 shows the result for a different accelerator voltage, $\Phi_a = -120$V. In figures 12 and 13 we keep the same operating condition (accelerator voltage: -180V; beamlet current: 0.27mA/hole) but vary the geometric parameters Fig.12 shows the results for two difference accelerator hole diameters, $d_a = 1.44$mm in Fig.12a, and $d_a = 1.64$mm in Fig.12b. Fig. 13 shows the result for a different gap size, $L = 0.3$mm.

In Fig.14, we show the saddle point potential Φ_s obtained from particle simulations of the NSTAR ion optics as a function of the accelerator hole diameter for two beamlet currents, 0.27 mA/hole and 0.21 mA/hole. The results are grouped according to accelerator voltage Φ_a.

Not surprisingly, the saddle point potential Φ_s rises as one increases the beamlet current, reduces the magnitude of the accelerator voltage, or increases the accelerator hole diameter. For instance, for a 0.27mA/hole beamlet current, the saddle point potential for the case of nominal condition is $\Phi_s \simeq -47$V (Fig.9). When Φ_a is lowered to -120V, $\Phi_s \simeq -3.8$V (Fig.11). At hole size $d_a = 1.44mm$, $\Phi_s \simeq -3.5$V (Fig.12a). Considering that the downstream electron temperature $T_{e\infty} \simeq 1.5$eV, the saddle point potential in Fig.11 and Fig.12a is high enough to allow a significant number of electrons to backflow. At hole size $d_a = 1.64mm$, we find that $\Phi_s \simeq +1.2$V (Fig.12b). This essentially allows a free streaming of downstream electrons toward the accelerator system.

From these potential fields, we can estimate the backstreaming electron current. We assume that the downstream electrons follow a Maxwellian distribution. When the relative potential in the accelerator grid aperture is negative, the only electrons which will be able to backstream are the electrons in the high energy tail of the Maxwellian distribution. Thus, the backstreaming electron current density is given by

$$J_{eb} = en_\infty \sqrt{\frac{T_{e\infty}}{2\pi m_e}} \exp(\frac{\Phi}{T_{e\infty}}), \quad \Phi < 0 \qquad (12)$$

When the potential becomes positive, all of the electrons in the Maxwellian distribution can free streaming into the discharge chamber. To compute the total electron backstreaming current through an accelerator grid aperture, the backstreaming current density must be integrated over the surface through which electrons backstream:

$$I_{eb} = \int J_{eb} dA \qquad (13)$$

The saddle point located at the minimum voltage along the axis of the accelerator grid hole lies on this backstreaming surface. The surface follows the path of steepest voltage decent away from the saddle point. The envelop of this surface is determined from the potential field from particle simulations. Performing this integral gives the total electron backstreaming current through a single accelerator grid aperture. Fig.15 shows the electron backstreaming current as a function of accelerator grid voltage for two beamlet currents, 0.21mA and 0.27mA.

During the 8000 hour NSTAR ion engine endurance test performed at JPL, the electron backstreaming limit is measured at various stages of the tests. The electron backstreaming limit is defined as the accelerator voltage at which the electron backstreaming current was 1% of the total beam current. Fig.15 shows the measured electron backstreaming limit as a function of the test run time. At the beginning of the test, the accelerator hole diameter d_a is measured to be about 1.10 to 1.14mm. At the end of the test, the accelerator hole diameter d_a is measured to be about 1.40 to 1.47mm.

The measured electron backstreaming current is the sum of the currents through each of the ion optics apertures, while we have only considered a single aperture in our backstreaming calculation. Nevertheless, it is still interesting to make some comparisons between our calculations and the measured results. We shall make two comparisons. In the first comparison, we calculate the backstreaming electron current from eq(13) and find the the accelerator voltage at which the electron backstreaming current I_{eb} reaches 1% of the beamlet current through a single aperture, I_b:

$$I_{eb}(\Phi_a) \geq 0.01 I_b \qquad (14)$$

In the second comparison, we only calculate the backstreaming current density from eq(12) and find the the accelerator voltage at which the electron backstreaming current density at the saddle point, J_{ebs}, becomes larger

than 1% of the beamlet current density through a single aperture, J_b:

$$J_{ebs}(\Phi_a) = en_\infty \sqrt{\frac{T_{e\infty}}{2\pi m_e}} \exp(\frac{\Phi_s}{T_{e\infty}}) \geq 0.01 J_b \qquad (15)$$

Eq(15) ties directly the saddle point potential Φ_s to the backstreaming onset.

The results are shown in Fig.17. Results for condition eq(14) are shown by the dashed line and that for condition eq(15) are shown by the dotted line. On Fig.17, we also include the measured backstreaming limit for the two known accelerator diameters from the NSTAR 8000 hour test, point A, measured at the beginning of the test, and point B, measured at the end of the test. We find that the calculated backstreaming limit derived from both eq(14) and eq(15) are in reasonable agreement with the test data. Since the particle simulations from which the calculated backstreaming limit is derived include neither the downstream charge exchange ions nor any back facility ions, it is not surprising that the calculations underpredicts the backstreaming limit at smaller hole diameter. The result also suggests that one may make a reasonable prediction of the backstreaming onset based on consideration of electron current density at the saddle point.

4. Summary and Conclusions

In summary, fully three-dimensional numerical models based on particle-in-cell with Monte Carlo collisions (PIC-MCC) simulations are developed to study ion optics plasma flow. Out of considerations for computational efficiency for large-scale simulations, this code is build upon the standard orthogonal grids and a finite-difference based formulation. The 3-D optics aperture geometry is handled by a method of sub-gridscale placement of boundaries which explicitly includes the location of the optics wall in relation to the grid in the finite-difference form of Poisson's equation. Multiple apertures may be included explicitly in the simulation domain.

This 3-D particle simulation model is applied to analysis the onset of electron backstreaming, a potential failure mode for the NSTAR ion engine. The onset of electron backstreaming is investigated by studying the the structure of the electric potential near the accelerator gird as a function of accelerator voltage, beamlet current, and optics geometric parameters. The potential field obtained from particle simulations are utilized to calculate the backstreaming electron current and the backstreaming limit. Although this analysis is performed for a single aperture, the calculated backstreaming onset is in reasonable agreement with the measured data. More over, we show that one may make a reasonable prediction of backstreaming onset based on the electron current density and potential at the saddle point, which can be readily obtained from ion optics simulations.

Acknowledgement

This work was carried out by the Jet Propulsion Laboratory, California Institute of Technology under a contract with NASA. Access to the Cray supercomputers used in this study was provided by funding from NASA Offices of Mission to Planet Earth, Aeronautics, and Space Science.

References

[1] Y. Arakawa and M. Nakano, An efficient three-dimensional optics code for ion thruster research, *AIAA 96-3198*, 1996.

[2] R. Bond and P. Latham, Ion thruster extraction grid design and erosion modeling using computer simulation *AIAA 95-2923*, 1995.

[3] D. Grote, Three-dimensional simulations of space-charge dominated heavy ion beams with applications to inertial fusion energy, Ph.D. thesis, University of California, Davis, 1994.

[4] Y. Hayakawa, Three-dimensional numerical model of ion optics system, *J. Propulsion and Power*, 8(1), 1992, pp.110.

[5] X. Peng, W. Ruyten, and D. Keefer, Three-dimensional particle simulation of grid erosion in ion thrusters, *IEPC 91-119*, 1991.

[6] X. Peng, D. Keefer, and W. Ruyten, Plasma particle simulation of electrostatic ion thrusters, *J. Propulsion and Power*, 8(2), 1992, pp.361.

[7] X. Peng, W. Ruyten, V. Friedly, D. Keefer, and Q. Zhang, Particle simulation of ion optics and grid erosion for two-grid and three-grid systems, *Rev. Sci. Instrum.*, 65(5), 1994, pp1770.

[8] T. Shiraish, H. Kuninaka, S. Satori, and K. Kuriki, Numerical simulation of grid erosion for ion thruster *IEPC 95-90*, 1995.

[9] D. Rapp and W. Francis, Charge-exchange between gaseous ions and atoms, *J. Chem. Phys.*, 37, 1962, p2631.

[10] V. Rawlin, Erosion characteristics of two-grid ion accelerating systems, *IEPC 93-175*, 1993.

[11] J. Wang,D. Kondrashov, P. Liewer, and S. Karmesin, Three-dimensional deformable grid electromagnetic particle-in-cell for parallel computers, submitted to *J. Plasma Physics*, 1998.

[12] T. Westermann, Localization schemes in 2D boundary-fitted grids, *J. Computational Physics*, 101, 1992, pp307.

Figure Captions

Figure 1: 3-D simulation domain.

Figure 2: Sub-gridscale placement of boundaries.

Figure 3: Cross section of the simulation domain used for the example run.

Figure 4: Potential contours and electric field vectors on a x-y plane downstream of the accelerator grid.

Figure 5: Potential contours on the z-y surface at $x = 0$ (a) and the z-x surface at $y = 0$ (b).

Figure 6: Ion current density vectors (a) and ion velocity vectors (b) on the z-x surface at $y = 0$.

Figure 7: Position (a) and phase space (b) plots for the propellant beam ions.

Figure 8: Position (a) and phase space (b) plots for the charge-exchange ions.

Figure 9: Potential contours for the nominal geometric and operating parameters of the NSTAR engine listed in Table 1. Contour levels are 0, -50, -100, -150, and -47 (Φ_s) V.

Figure 10: Potential contours for zero beamlet current (a) and 0.21 mA/hole beamlet current (b). Contour levels are 0, -50, -100, -150 V and Φ_s. $\Phi_s = -126$ V in (a) and -62.5 V in (b).

Figure 11: Potential contours for $\Phi_a = -120$ Volts Contour levels are 0, -50, -100, and -3.85 V.

Figure 12: Potential contours for $d_a = 1.44$ mm (a) and $d_a = 1.64$ mm (b). Contour levels are 0, -50, -100, -150 V, and Φ_s. $\Phi_s = -3.5$ V in (a) and 1.2 V in (b).

Figure 13: Potential contours for $g = 0.3$ mm Contour levels are 0, -50, -100, -150, and -41 Volts.

Figure 14: Saddle point potential Φ_s vs. accelerator hole diameter for beamlet current 0.27 mA (a) and 0.21 mA/hole (b). Φ_s are grouped by accelerator voltage $\Phi_a = -210$, -180, -150, -120, and -90 V.

Figure 15: Analytically calculated backstreaming electron current.

Figure 16: Electron backstreaming limit measured during the NSTAR 8000 hour endurance test.

Figure 17: Comparison of the calculated electron backstreaming limit and the NSTAR data (points A and B). The dashed lines are based on calculations of single aperture backstreaming electron current. The dotted lines are based on electron current density at the saddle point.

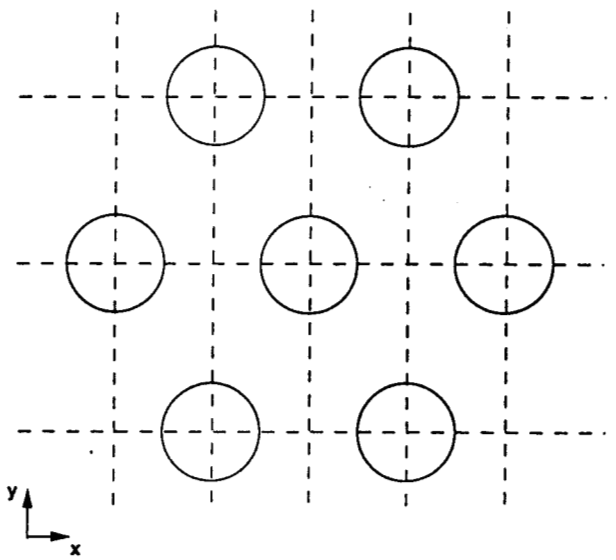

Figure 1

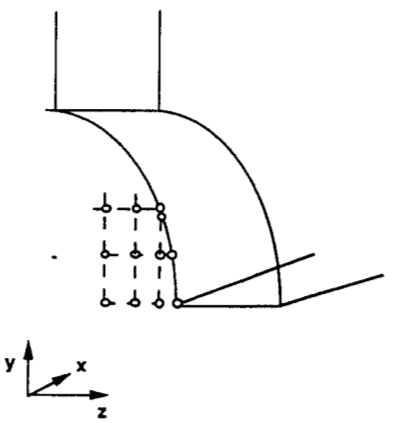

Figure 2

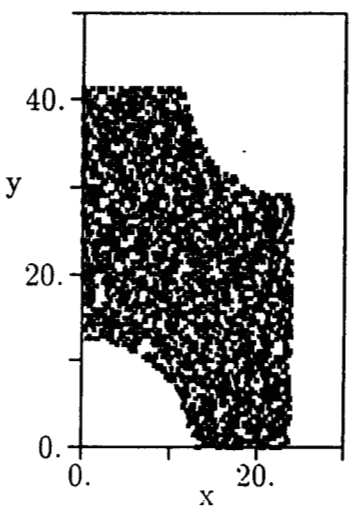

Figure 3

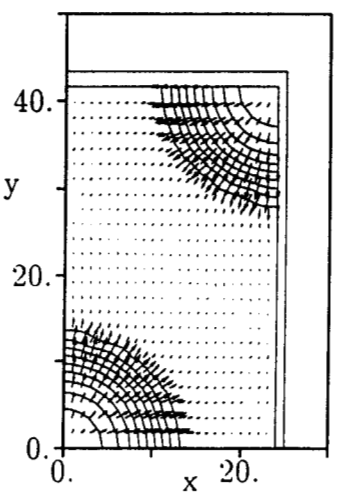

Figure 4

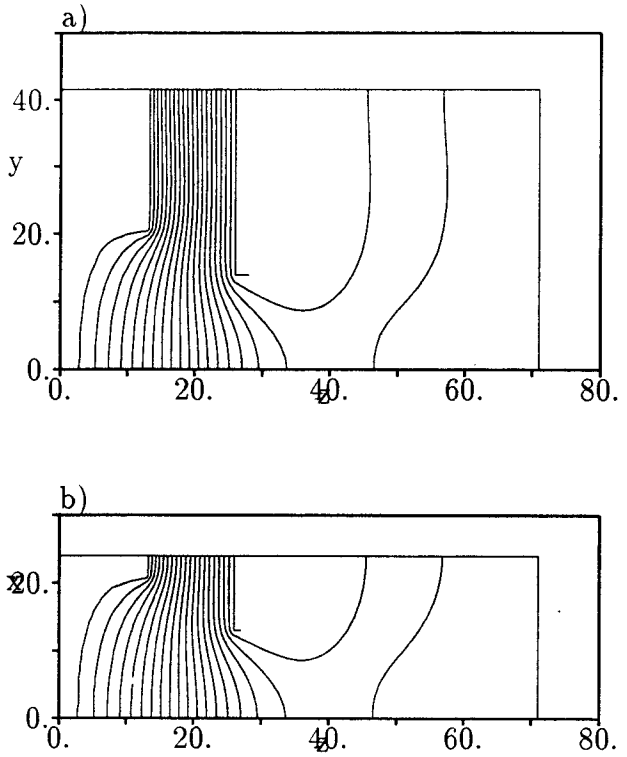

Figure 5

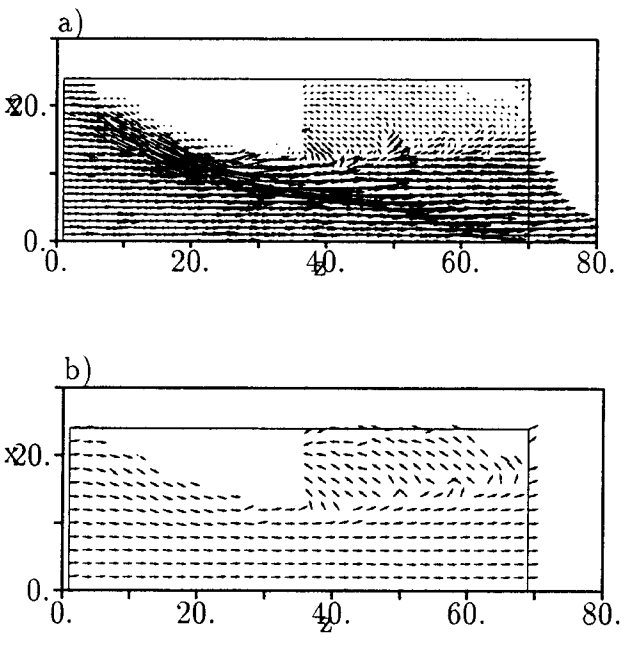

Figure 6

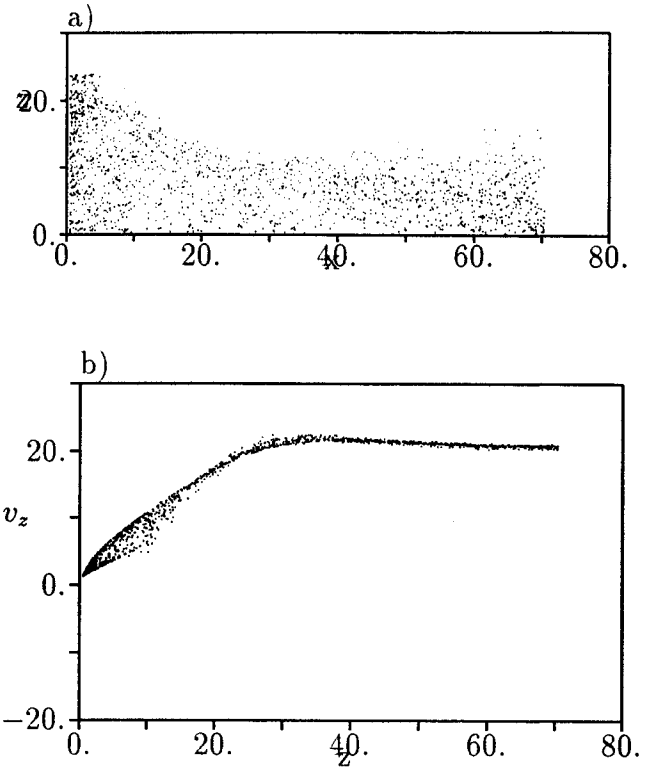

Figure 7

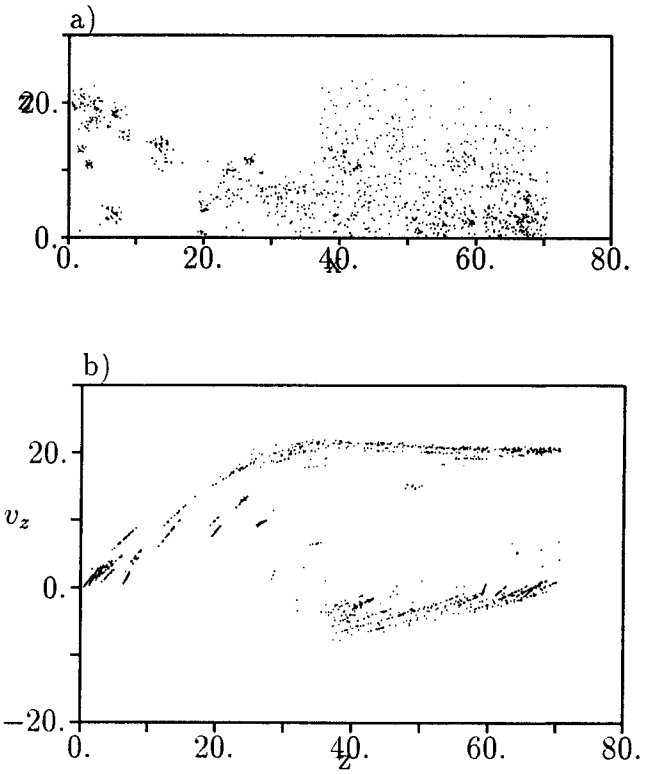

Figure 8

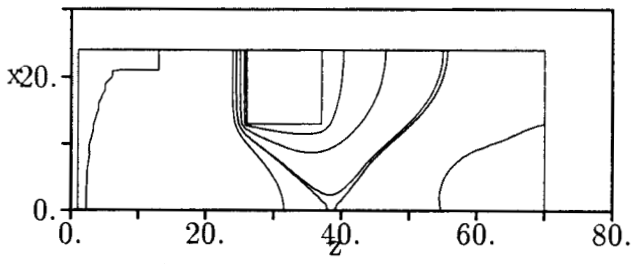

Figure 9

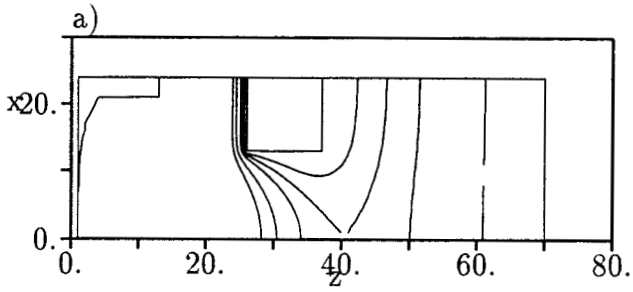

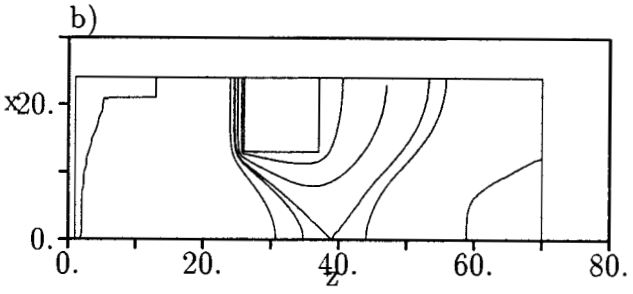

Figure 10

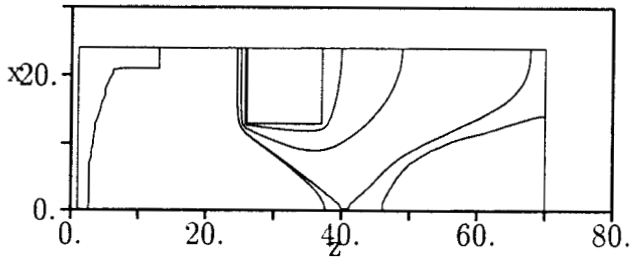

Figure 11

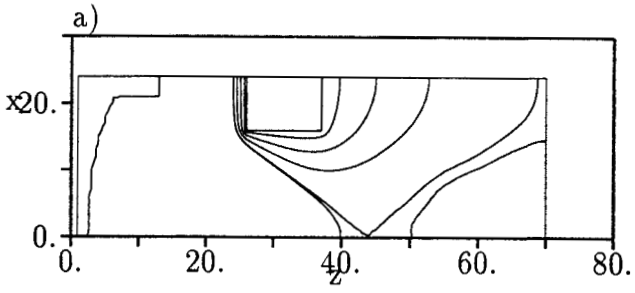

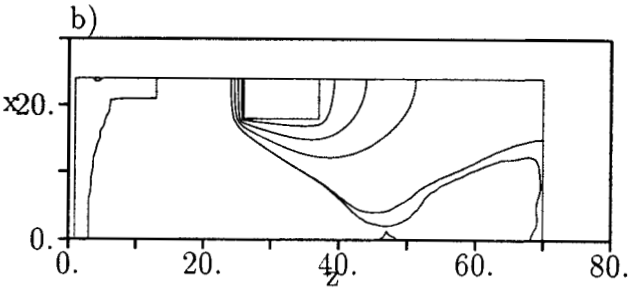

Figure 12

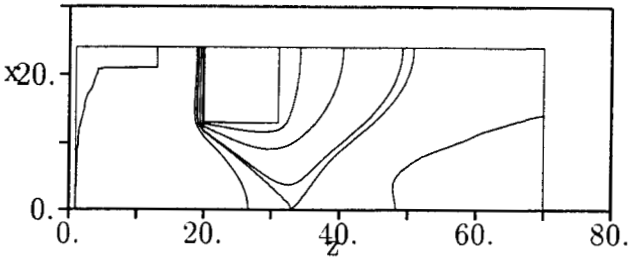

Figure 13

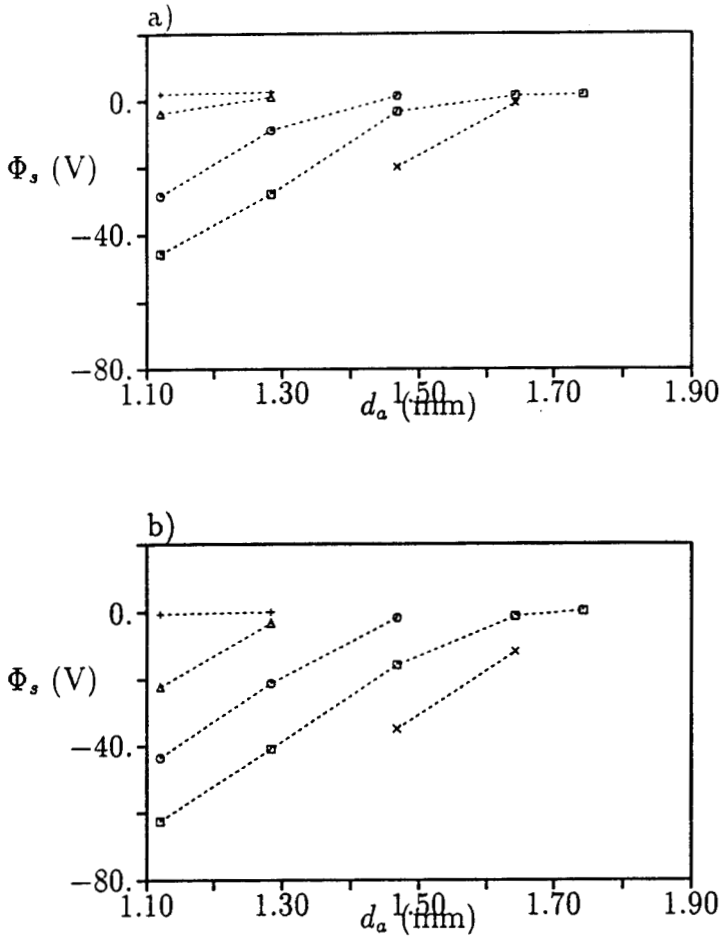

Figure 14

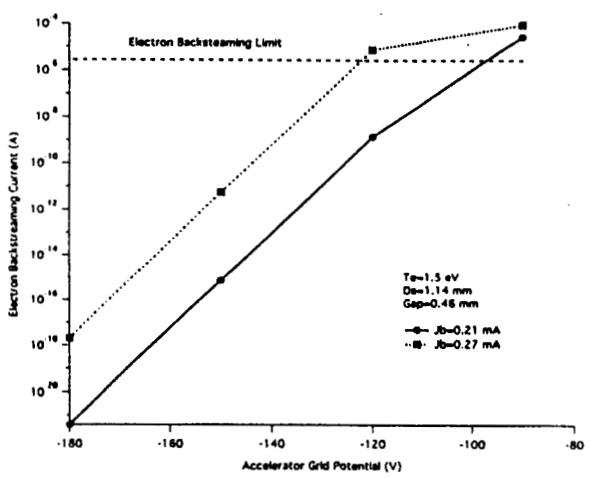

Figure 15

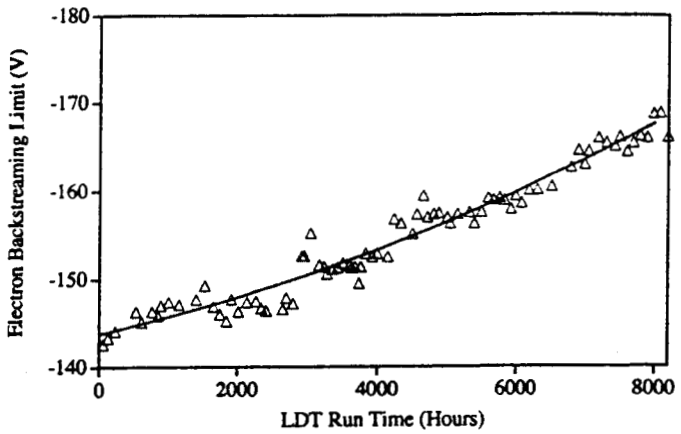

Figure 16

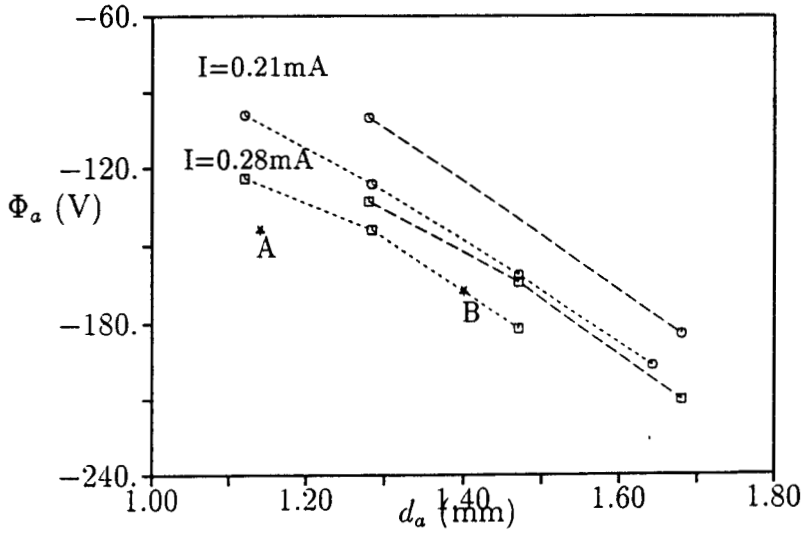

Figure 17